OPEN ACCESS
IOP Publishing
Plasma Sources Science and Technology
Plasma Sources Sci. Technol. **33** (2024) 045019 (13pp)
https://doi.org/10.1088/1361-6595/ad3c69

Electron power absorption in CF_4 capacitively coupled RF plasmas operated in the striation mode

Ranna Masheyeva[1,2,*], Mate Vass[1,3], Xiao-Kun Wang[3,4], Yong-Xin Liu[4], Aranka Derzsi[1], Peter Hartmann[1], Julian Schulze[3] and Zoltán Donkó[1]

[1] Institute for Solid State Physics and Optics, HUN-REN Wigner Research Centre for Physics, 1121 Budapest, Hungary
[2] Department of General Physics, Satbayev University, 050013 Almaty, Kazakhstan
[3] Chair of Applied Electrodynamics and Plasma Technology, Faculty of Electrical Engineering and Information Sciences, Ruhr University Bochum, 44801 Bochum, Germany
[4] Key Laboratory of Materials Modification by Laser, Ion, and Electron Beams (Ministry of Education), School of Physics, Dalian University of Technology, 116024 Dalian, People's Republic of China

E-mail: ranna.masheyeva@wigner.hu

Received 16 January 2024, revised 8 March 2024
Accepted for publication 9 April 2024
Published 3 May 2024

Abstract

The electron power absorption mechanisms in electronegative capacitively coupled plasmas in CF_4 are investigated using particle-in-cell/Monte Carlo collisions simulations at a pressure of $p = 60$ Pa, a driving frequency of $f = 13.56$ MHz for voltage amplitudes in the interval of $\phi_0 = 100-300$ V, where pronounced self-organized density variations, i.e. striations, develop. The calculations are based on the Boltzmann term analysis, a computational diagnostic method capable of providing a complete spatio-temporal description of electron power absorption. The discharge undergoes an electron power absorption mode transition from the drift-ambipolar- to the striation-mode at $\phi_0 = 180$ V. Although Ohmic power absorption is found to be the dominant electron power absorption mechanism in the parameter range considered, the electron power absorption mode transition can be inferred from the behaviour of the spatio-temporally averaged ambipolar power absorption as a function of the voltage amplitude. Furthermore, it is shown, that as a consequence of the presence of striations, the temporal modulation of the electron density leads to a temporal modulation of the ambipolar electric field, which is responsible for the striated structures of various physical quantities related to electrons, such as the electron temperature and the ionization source function.

Keywords: electron power absorption, capacitively coupled plasma, Boltzmann term analysis, particle in cell simulation

* Author to whom any correspondence should be addressed.

1. Introduction

Low temperature capacitively coupled radio frequency (CCRF) discharges are extensively used in a variety of modern applications, such as plasma etching and deposition in the semiconductor industry and surface treatment in biomedical plasma applications [1–3]. The knowledge-based control and optimization of these plasma processes require an understanding of the physical mechanisms present in such systems, in particular, those responsible for the energy gain and loss of electrons, i.e. the *electron power absorption mechanisms* [4]. These mechanisms are essential in discharge plasmas, as electrons need to gain energy from the electric field to be able to participate in ionization and to generate process relevant particle species such as radicals [2, 5].

A unified and exact treatment of electron power absorption, based on the momentum balance equation of the electrons, assisted by particle-in-cell/Monte Carlo collisions (PIC/MCC) simulations was first proposed by Surendra and Dalvie [6]. This method is capable of providing a self-consistent, spatio-temporally resolved description of electron power absorption in CCRF discharges, and is termed *Boltzmann term analysis* [7, 8]. The Boltzmann term analysis has recently been used to investigate electron power absorption in CCRF discharges operated in low pressure inert gases [4, 7, 9, 10], reactive gases [8, 11–13], also in the presence of an external magnetic field [14–16], as well as in atmospheric microplasma jets [17] and in Hall thrusters [18–20]. This method has provided a deeper understanding of the underlying physical mechanisms of electron power absorption. Based on the work of Schulze *et al* [7], it was shown that the reason for 'collisionless heating' at low pressure (called pressure heating in the framework of the Boltzmann term analysis) is a self-amplifying mechanism leading to a temporal asymmetry in the kinetic electron temperature, which causes a nonzero electron power absorption on time average, that can be dominant as the background gas pressure is decreased. This mechanism can be mitigated, however, leading to situations where Ohmic power absorption is dominant at low pressures, as shown in [8, 10].

These fundamental insights into electron power absorption are intimately linked to various modes of discharge operation such as the $\alpha-$ [21–24], $\gamma-$ [25–28], drift-ambipolar (DA-) [29–31], and striation (STR-) modes [32–36]. Electropositive discharges commonly operate in either the α-mode or in the γ-mode [22, 27, 28]. In the α-mode, electrons are accelerated by electric fields during the time of sheath expansion within each RF period. Consequently, the ionization rate peaks in the vicinity of the edge of the expanding sheath. In the γ-mode, on the other hand, ionization is primarily maintained by secondary electrons emitted from the electrodes due to the ion bombardment and accelerated by the strong electric field at times of high sheath voltages as well as their collisional multiplication inside the sheaths. As a result, most of the ionization occurs near the edges of the fully expanded sheaths. Besides these modes, another electron power absorption mode, termed as the 'DA- mode', is characteristic for electronegative discharges [29–31], where the electron density is strongly depleted in the bulk plasma. As a consequence of this, a drift electric field builds up in the bulk region which accelerates the electrons. Additionally, due to the specific spatial electron density profile (exhibiting local maxima at the sheath edges, i.e. electropositive edges) strong ambipolar fields also develop near the sheath edges. Since the first work where the existence of the different modes has been reported [37], the transitions between these distinct power absorption modes have been documented in various gases based on changing the gas pressure, radio frequency voltage, and driving frequency. The transition between the α- and γ- modes has been investigated experimentally [38, 39] as well as numerically [28, 40]. The transition between the DA- and α-modes has been demonstrated depending on changes in gas pressure [29, 31, 41–43], electrode gap [43], driving frequency [41, 44], voltage waveform [29, 41, 45, 46] and external magnetic fields [14, 47].

For most of the usual operating conditions, CCRF gas discharges exhibit a homogeneous plasma bulk region. For some gases and operating conditions, however, strong density modulations, i.e. 'striations', can spontaneously be generated [1, 48]. Such structures typically build up in plasmas operated in electronegative molecular gases e.g. in CF_4, where the bulk plasma is dominated by positive and negative ions and are observed at relatively low driving frequencies where both of these ionic species can react to the temporal variations of the electric field [48, 49]. The development of these distinctive structures is related to the periodic acceleration of ions by the RF electric field. As ions move, they generate local space charges, inducing a spatial modulation of the electric field. This modulation significantly impacts the rate of electron heating and subsequently influences the ionization rate. Consequently, when the ion number density reaches a critical threshold at a specific position within the plasma bulk, allowing ions to respond to the RF electric field and to generate space charges, there is a notable increase in the ionization rate in that vicinity. Striations (either moving or stationary) have comprehensively been studied in RF plasma sources and also in DC discharges in a wide range of discharge conditions, from low pressure [29, 33, 48, 50] to moderate [51, 52] and atmospheric pressures [53, 54]. Fluid [55, 56] as well as kinetic [33–36, 48, 50, 52, 53, 57, 58] models have been used for the understanding of the formation of striations.

In the work of Liu *et al* [33], experimental and computational studies as well as a supporting theoretical (ion-ion plasma) model were presented for a CF_4 CCRF discharge. In this study, the discharge was driven by an RF voltage with a frequency of 8 MHz. The spatio-temporal distribution of the electron impact excitation rate was monitored by phase resolved optical emission spectroscopy (PROES). These observations were reproduced and analyzed by PIC/MCC simulations. The positive and negative ion (CF_3^+ and F^-) densities were sufficiently high so that ions, due to their increased plasma frequency, could follow the temporal changes of the bulk electric field. The movement of positive and negative ions

in opposite directions in response to the time-modulated bulk electric field results in the formation of spatially alternating space charges and electric field patterns within the plasma bulk. These striated space charge distributions amplify or weaken the local bulk electric field depending on the local polarity of the space charge. This feedback mechanism leads to the formation of the self-organized striped patterns in light emission, as electrons gain high energy due to the strong, spatially modulated bulk electric field.

More detailed investigations of effects of the pressure, driving voltage, and electrode gap on the formation of striations have been carried out in [34, 36] based on PROES measurements, PIC/MCC simulations, and an ion-ion plasma model. The authors found that the striation gap, i.e. the distance between two ion density peaks, is inversely proportional to the driving frequency and the gas pressure, while it weakly depends on the RF voltage and the electrode gap. Transitions between 'striated' and 'non-striated' modes have been found to be controlled by the gas pressures or the RF voltage. The above studies using single-frequency (SF) excitation of the CCRF discharges were extended in [35, 58] to the case of dual-frequency excitation: 8/40 MHz and 2/10 MHz. The properties of striated structures of different plasma parameters in a dual-frequency discharge and the effect of the high-frequency voltage amplitude on the striated structures and charged species densities were studied at a gas pressure of 100 Pa in [35]. It was found that the high-frequency voltage amplitude leads to a decrease of the number of striations and finally to their disappearance. In the 8 MHz/40 MHz case, the ions could not respond to the high frequency modulation [35]. Meanwhile, in [58] a frequency pair of 2 MHz and 10 MHz was chosen to ensure that ions can react to both frequencies. We note that striations were also observed recently in the positive column of a CF_4 DC discharge [59].

In this work, we investigate the peculiarities of the electron power absorption mechanisms in electronegative CCPs in CF_4 in the striation mode. The calculations are based on the Boltzmann term analysis method of the electron momentum balance equation, which is integrated into a PIC/MCC simulation code of the discharge. Our calculations are carried out at a fixed gas pressure and frequency and cover a range of voltage amplitudes where a transition from the DA- to the STR- mode can be followed.

The paper is structured as follows: section 2 describes the Boltzmann term analysis method and provides details about the simulation approach applied in this paper. In section 3, the results are presented and discussed. Finally, in section 4, conclusions are drawn.

2. Computational method and theoretical background

Our numerical studies are based on a one-dimensional in space and three-dimensional in velocity space (1d3v) electrostatic PIC/MCC code [60, 61], which has been validated against experiments [33]. The simulations are performed in CF_4 with a fixed electrode gap of $L = 15$ mm and a radio frequency driving voltage amplitude in the range of 100–300 V. The plasma is excited by a single-frequency waveform $\phi(t) = \phi_0 \cos(2\pi ft)$, with $f = 13.56$ MHz at a pressure of 60 Pa. The driving voltage is applied to the electrode situated at $x = 0$ and the electrode at $x = L$ is grounded. For the surface model of the electrodes a constant electron reflection coefficient of $R = 0.7$ and a positive ion-induced secondary electron emission coefficient (SEEC) of $\gamma = 0.01$ is assumed [62]. The temperature of the background gas is held at $T_g = 350$ K. A spatial resolution of $N_x = 1000$ grid points and a temporal resolution of $N_t = 8000$ timesteps per RF period are used to ensure the stability of the simulation and good numerical accuracy of the results. The discharge parameters (pressure and electrode gap) were chosen such that by changing the voltage the discharge undergoes a power absorption mode transition from the DA- to the STR-mode.

In the simulation electrons, CF_3^+, CF_3^-, and F^- ions are traced, which have been identified as dominant species in earlier studies [63, 64]. These ions are created in $e^- + CF_4$ collisions, listed in table 1. $e^- + CF_4$ collisions that result in the formation of other charged particle species are also included according to table 1 by taking into account their effects on the electron kinetics via the corresponding losses of the electron's kinetic energy, but the products are not traced. The collision cross sections for $e^- + CF_4$ collisions are the same as those used in [65], originally taken from [66], except for the electron attachment processes that yield CF_3^- and F^- ions, for which we have used data from Bonham [67].

In the case of ion-molecule reactions occurring in CF_4 plasmas, there exist numerous possible channels and a large number of reaction processes could be taken into account in the simulation for the $CF_3^+ + CF_4$, $F^- + CF_4$, and $CF_3^- + CF_4$ collisions [63, 64, 68]. The collisions can be both of elastic and reactive nature. In the case of elastic ion-molecule collisions, a Langevin-type cross section is used, an isotropic channel and an anisotropic channel are distinguished based on the impact parameter that is chosen in a random manner. In the case of reactive collisions the type of impacting ion may be conserved or another ionic species can be created as a consequence of the interaction between the projectile and the target (CF_4 molecule) species. Table 2 lists the first few (lowest threshold energy) processes for each of the projectiles: CF_3^+, F^-, CF_3^-, while in the simulation the full sets of reactions comprising 41, 19, and 67 channels, respectively, for the above ionic species are included. The cross sections of some of the ion-impact processes are presented in figure 1. The panels include the cross sections of the anisotropic and isotropic parts of the elastic scattering as well as the cross sections of some representative reactions listed in table 2. (For a full list of reactions see tables II–IV of [69].) Similarly to the case of $e^- + CF_4$ collisions, here we disregard as well the infrequent formation of lighter positive ions CF_2^+, CF^+, C^+ and F^+. In the processes that yield these species as products the incoming projectile ion is kept instead, to ensure charge conservation.

Recombination processes between electrons and CF_3^+ as well as positive and negative ions are included according to

Table 1. List of $e^- + CF_4$ collisions considered in the model. ΔE is the energy threshold in the center of mass coordinate system.

#	Process	Collision type	ΔE (eV)
1	$e^- + CF_4 \longrightarrow e^- + CF_4$	Elastic scattering	0
2	$e^- + CF_4 \longrightarrow e^- + CF_4(v=1)$	Vibrational excitation	0.108
3	$e^- + CF_4 \longrightarrow e^- + CF_4(v=3)$	Vibrational excitation	0.168
4	$e^- + CF_4 \longrightarrow e^- + CF_4(v=4)$	Vibrational excitation	0.077
5	$e^- + CF_4 \longrightarrow e^- + CF_4^*$	Electronic excitation	7.54
6	$e^- + CF_4 \longrightarrow 3e^- + CF_3^{++} + F$	Dissociative ionization	41
7	$e^- + CF_4 \longrightarrow 2e^- + CF_3^{+} + F$	Dissociative ionization	16
8	$e^- + CF_4 \longrightarrow 3e^- + CF_2^{++} + 2F$	Dissociative ionization	42
9	$e^- + CF_4 \longrightarrow 2e^- + CF_2^{+} + 2F$	Dissociative ionization	21
10	$e^- + CF_4 \longrightarrow 2e^- + CF^{+} + 3F$	Dissociative ionization	26
11	$e^- + CF_4 \longrightarrow 2e^- + C^{+} + 4F$	Dissociative ionization	34
12	$e^- + CF_4 \longrightarrow 2e^- + F^{+} + CF_3$	Dissociative ionization	34
13	$e^- + CF_4 \longrightarrow F^- + CF_3$	Attachment	5
14	$e^- + CF_4 \longrightarrow CF_3^- + F$	Attachment	5
15	$e^- + CF_4 \longrightarrow e^- + CF_3 + F$	Neutral dissociation	12
16	$e^- + CF_4 \longrightarrow e^- + CF_2 + 2F$	Neutral dissociation	17
17	$e^- + CF_4 \longrightarrow e^- + CF + 3F$	Neutral dissociation	18

Table 2. Examples of ion-CF_4 molecule collision processes included in the simulation. ΔE is the threshold energy in the center of mass coordinate system. For each pair of the collision partners, only a few of the processes are listed. For more information see the text.

#	Reaction	Products	ΔE (eV)
1.1	$CF_3^+ + CF_4 \rightarrow$	$CF_3^+ + CF_3 + F$	5.621
1.2		$CF_2^+ + CF_4 + F$	5.843
1.3		$CF^+ + CF_4 + F_2$	7.546
1.4		$CF_3^+ + CF_2 + F_2$	7.598
1.5		$F^- + CF_4 + 2F$	9.146
...		...	...
2.1	$F^- + CF_4 \rightarrow$	$CF_4 + F + e^-$	3.521
2.2		$F^- + CF_3 + F$	5.621
2.3		$CF_3 + F_2 + e^-$	7.542
2.4		$F^- + CF_2 + F_2$	7.598
2.5		$CF_3 + 2F + e^-$	9.142
...		...	...
3.1	$CF_3^- + CF_4 \rightarrow$	$CF_4 + CF_3 + e^-$	1.871
3.2		$F^- + CF_4 + CF_2$	1.927
3.3		$CF_4 + CF_2 + F + e^-$	5.448
3.4		$CF_3^- + CF_3 + F$	5.621
3.5		$2CF_3 + F + e^-$	7.492
...		...	...

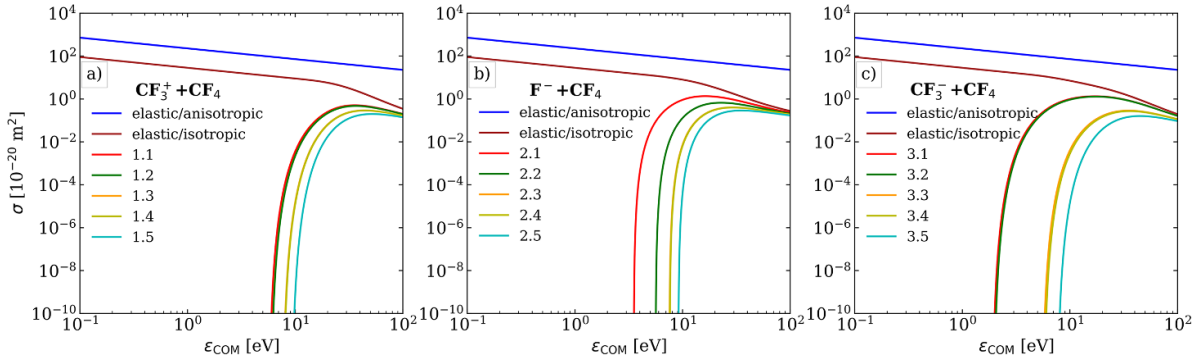

Figure 1. Cross sections of the elastic and a few representative inelastic ion-molecule collision processes in CF_4 as a function of the kinetic energy in the center-of-mass (COM) frame. The labeling of the curves corresponds to the indexes of the processes in table 2.

Table 3. Recombination processes considered in the simulation and the corresponding rate coefficients, where the ion and electron temperatures, T_i and T_e, respectively, are in units of eV.

Reaction	Rate coefficient ($m^3 s^{-1}$)
$CF_3^+ + e^-$	$3.95 \times 10^{-15} T_i^{-1} T_e^{-0.5}$
$CF_3^+ + F^-$	1×10^{-13}
$CF_3^+ + CF_3^-$	1×10^{-13}

the procedure described in [70, 71]. The recombination processes and the recombination rate coefficients used in the simulation are listed in table 3. The rate coefficients for the ion-ion recombination are taken from [72], and those for $e^- + CF_3^+$ from [70].

Information about the power absorption by the electrons is extracted from the simulation using the Boltzmann term analysis approach [4, 7, 10]. A comprehensive description of this method can be found in [4, 8, 10], we will briefly highlight here the key concepts only. The method is based on the spatially one-dimensional momentum balance equation for the electrons:

$$m_e \frac{\partial (n_e u_e)}{\partial t} + m_e \frac{\partial \left(n_e u_e^2\right)}{\partial x} = n_e e E_{tot} - \frac{\partial p_\parallel}{\partial x} - \Pi_c. \quad (1)$$

Here, e, m_e, n_e and u_e are the elementary charge, the electron mass, density and mean velocity, respectively. Meanwhile, $p_\parallel$ denotes the diagonal element of the pressure tensor for the electrons (here, 'parallel' refers to the direction of the discharge axis, which coincides with the direction of the electric field). Π_c is the electron momentum loss (arising as an effect of collisions between electrons and the atoms of the background gas), given by $\Pi_c = m_e n_e n_g \langle \sigma_m v v_x \rangle$, with n_g the gas density, σ_m the total momentum transfer cross section, and the angular brackets denote the ensemble average [73]. All quantities appearing in equation (1), except the electric field, are taken directly from the PIC/MCC simulation. The electric field, E_{tot} can be written as a sum, $E_{tot} = E_{in} + E_{\nabla p} + E_{Ohm}$, where the individual terms are given by

$$\begin{aligned} E_{in} &= -\frac{m_e}{n_e e}\left[\frac{\partial (n_e u_e)}{\partial t} + \frac{\partial \left(n_e u_e^2\right)}{\partial x}\right], \\ E_{\nabla p} &= \frac{1}{n_e e}\frac{\partial p_\parallel}{\partial x}, \\ E_{Ohm} &= -\frac{\Pi_c}{n_e e}. \end{aligned} \quad (2)$$

The inertial electric-field term E_{in} is the electric field needed to compensate for the change in the electrons' momentum. The ohmic field, E_{Ohm}, describes the electric field needed to account for the collisional momentum loss of electrons as a result of collisions with the background gas particles, while $E_{\nabla p}$, the electric field corresponding to the spatial gradient of the electron pressure, is usually divided into two separate electric field terms, according to $E_{\nabla p} = E_{\nabla n} + E_{\nabla T}$, where

$$\begin{aligned} E_{\nabla n} &= -\frac{T_\parallel}{n_e e}\frac{\partial n_e}{\partial x}, \\ E_{\nabla T} &= -\frac{1}{e}\frac{\partial T_\parallel}{\partial x}. \end{aligned} \quad (3)$$

In these equations $T_\parallel = p_\parallel / n_e = m_e \left(\langle v_x^2 \rangle - u_e^2\right)$ is the parallel electron temperature, which is a measure of the mean kinetic energy of the electron ensemble in its center of mass frame. Here, $E_{\nabla T}$ is the electric-field term originating from the spatial variation of the temperature, while $E_{\nabla n}$ is, in quasineutral regions, the 'classical ambipolar field'. After calculating the respective electric-field terms, the corresponding electron power absorption terms can be easily calculated by multiplying each of these with the electron conduction current density, j_c, i.e. $P_{tot} = E_{tot} j_c$, $P_{in} = E_{in} j_c$, $P_{Ohm} = E_{Ohm} j_c$, $P_{\nabla n} = E_{\nabla n} j_c$, $P_{\nabla T} = E_{\nabla T} j_c$.

3. Results

In this section, results are presented for a single-frequency excitation waveform at a fixed pressure of 60 Pa and a frequency of $f = 13.56$ MHz for voltage amplitudes in the range of $\phi_0 = 100$ V–300 V. The figures presented here include data, which were obtained by averaging the simulation results over 4000 RF cycles. (In our simulations, the striations appeared to be stable. We also did not observe large fluctuations of the number of superparticles over 80 000 RF-cycles.)

Simulation results for the time-averaged charged particle densities are presented in figure 2 for voltage amplitudes of 100 V (a), 160 V (b), 180 V (c), and 300 V (d), respectively. In all cases considered, the dominant species in the plasma bulk are CF_3^+ and F^- ions, while the electron density is depleted in this region, due to the presence of the negative ions. As a consequence of this, electropositive edges, i.e. local maxima of the electron density at the edges of the bulk region can be observed. As the voltage amplitude is raised to 160 V (panel (b)), the charged particle densities slightly increase, while near $\phi_0 = 180$ V (panel (c)) striations appear in the bulk, which lead to a spatial modulation of the charged particle densities. The amplitude of the striations increases with the voltage amplitude, as shown in panel (d) for $\phi_0 = 300$ V. The number of striations remains constant in the rather limited range of the parameters of our study, whereas over a wider range of voltage, pressure, and electrode gap, a varying number of these features was found in earlier studies [36]. As shown in panel (d), in case of striations, there is a shift between the maxima of the dominant ion species (CF_3^+ and F^-), and that of CF_3^-, in the sense that the striation maxima of CF_3^- are situated at the positions where the CF_3^+ and F^- densities are minimum. The reason for this is the recombination process between CF_3^+ and CF_3^- (see table 3), which leads to the destruction of CF_3^- whenever the CF_3^+ density is high, and the fact, that the cross

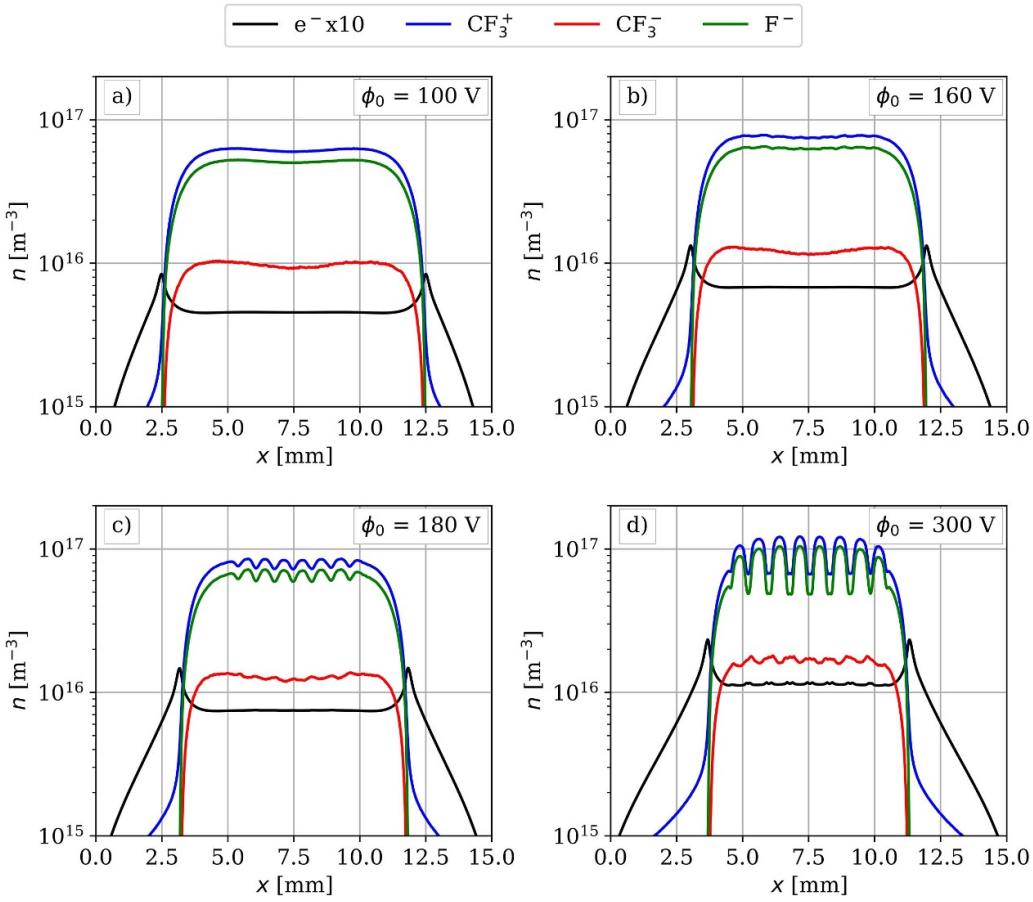

Figure 2. Time averaged charged particle density profiles for different values of the voltage amplitude, ϕ_0. (Note, that the data for the electron density are multiplied by a factor of 10.) Discharge conditions: $p = 60$ Pa, $f = 13.56$ MHz, $L = 15$ mm.

section for the creation of CF_3^- (process Nr. 14 in table 1) is a factor of 3 smaller than that of F^- [74]. The temporally averaged electron density exhibits local maxima near the edges of the density maxima of CF_3^+ and F^-. Although these maxima are barely visible in panel (d), since the increase takes place within a relatively small spatial region, the electron density gradients will be considerable, leading to an ambipolar field, which will determine the electron power absorption dynamics, as shown below.

The root mean square of the total electric field and the spatial distribution of the ion plasma frequencies of CF_3^+ and F^- ions ($\omega_\pm = \sqrt{e^2 n_\pm / \varepsilon_0 m_\pm}$, where e is the elementary charge, $n_\pm$ is the ion density, ε_0 is the permittivity of vacuum, and $m_\pm$ are the ion masses) are shown in figure 3 for two different voltage amplitudes, 100 V and 300 V. In panel (b), the driving frequency of 13.56 MHz is depicted as a gray dashed line. From panel (b), one can observe that the ion plasma frequencies become comparable to the driving frequency at $\phi_0 = 300$ V. Consequently, positive and negative ions are influenced by the RF alternating electric field, leading to the formation of space charges. The electric field resulting from these space charges either enhances or attenuates the local drift electric field within the bulk, causing a spatial modulation of both the electric field (figure 3(a)) and the ion densities (figures 2(c) and (d)).

In order to investigate the electron dynamics in more detail, figure 4 shows the spatio-temporal electron density distribution, n_e (a, b), and the total electron-impact ionization rate, S_{ion} (c, d) for a voltage amplitude of 100 V (left column) and 300 V (right column), respectively. The 100 V case exhibits all the characteristics of a discharge in the DA-mode [31]: (i) the electron density is depleted in the bulk with electropositive edges present at the positions of maximum sheath widths (panel (a)), and (ii) the ionization rate (panel (c)) is elevated in the bulk region, as a consequence of the high Ohmic power absorption due to the low electron density. The maxima of the electron density near the instantaneous sheath edges during sheath collapse at each electrode lead to a high electron density gradient, and, consequently, to a high ambipolar electric field, which can accelerate incoming electrons to high energies [8].

As the voltage amplitude is increased and striations appear, as shown in panel (b) because the ion densities and the ion plasma frequencies increase to high enough values so that the positive and negative ions can react to the instantaneous bulk electric field, the electron density in the bulk region becomes temporally modulated: The local electron density maxima, that form in the striation mode oscillate between two positions, corresponding to the edges of two adjacent striations in the ion density (cf figure 2(d)). This is the result of the creation of regions of positive space charges at the

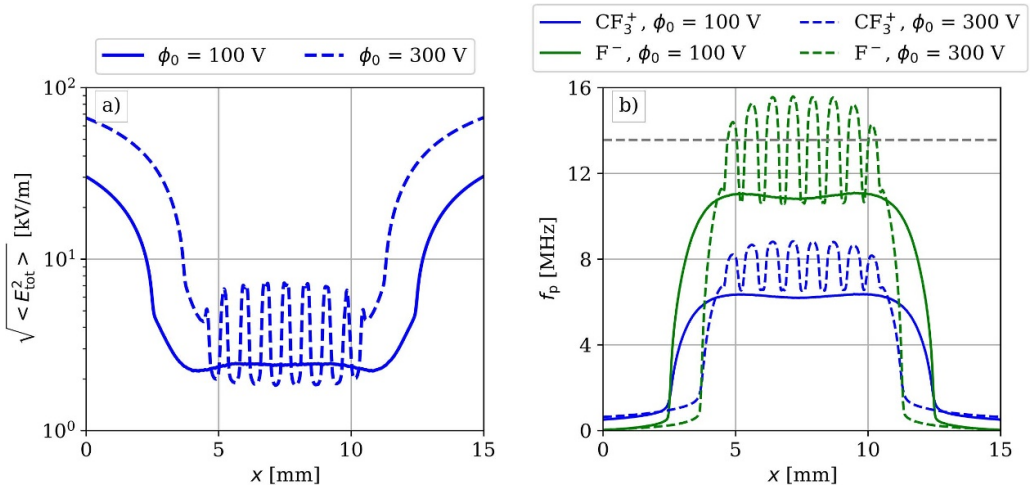

Figure 3. Root mean square of the total electric field (a) and spatial distributions of the plasma frequencies of CF_3^+ and F^- ions (b) in case of $\phi_0 = 100$ V and $\phi_0 = 300$ V.

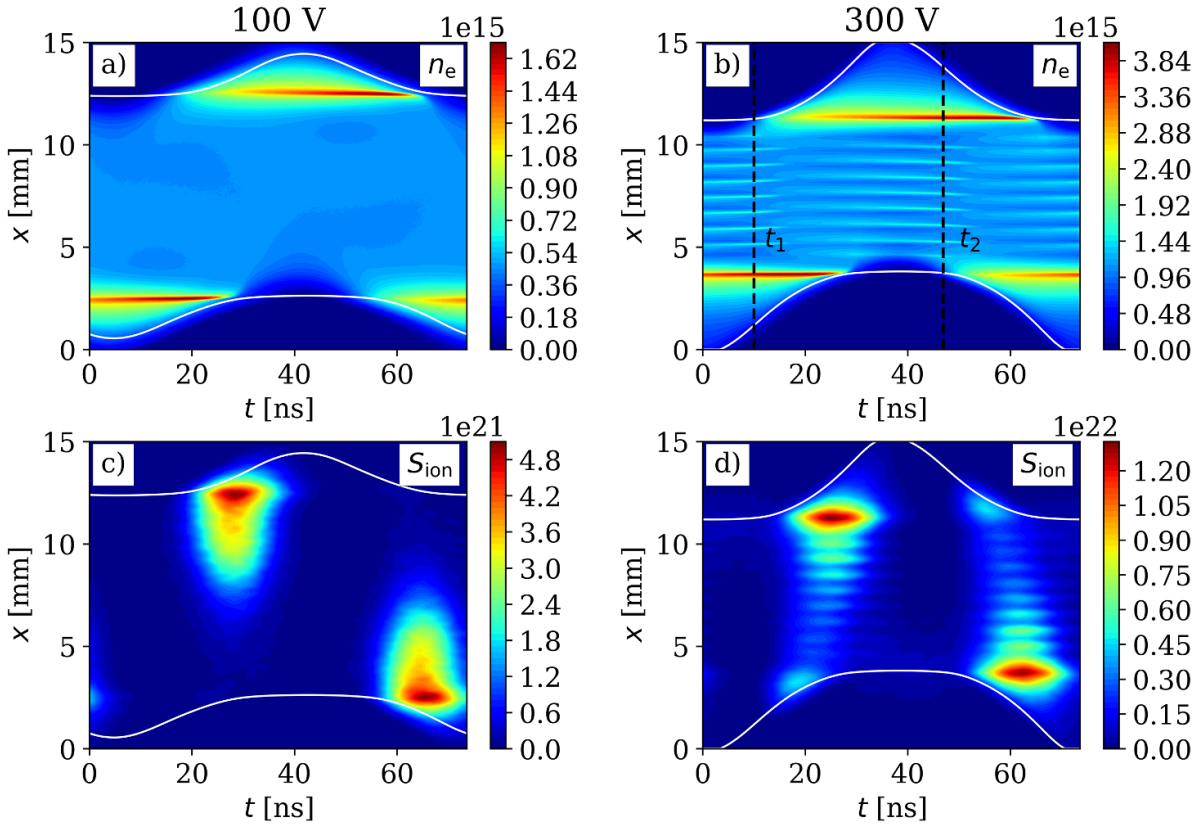

Figure 4. Spatio-temporal distributions of the electron density n_e (a) and (b) in units of m^{-3}, and electron-impact ionization rate, S_{ion} in units of $m^{-3}s^{-1}$ (c) and (d) for a voltage amplitude of 100 V (left column) and 300 V (right column). The solid white lines show the instantaneous sheath edge. The vertical dashed black lines in panel (b) represent two time instances half an RF-period apart: $t_1 \approx 10$ ns, $t_2 \approx 47$ ns, where the electron density maxima are close to their extreme positions in the frame of their oscillatory motion. Discharge conditions: $L = 15$ mm, $p = 60$ Pa, $f = 13.56$ MHz.

edges of the ion density maxima as the positive and negative ions move into opposite directions in response to the oscillating bulk electric field. Electrons move towards these regions of positive space charge and form local density maxima. The vertical dashed black lines in panel (b) indicate two time instances half an RF-period apart, between which the local maxima of the electron density move from one extreme position to the other. Due to the temporal modulation, the spatial distribution of the electron density, and, consequently, its gradient changes in time, which will lead to a temporal modulation of the ambipolar power absorption as well.

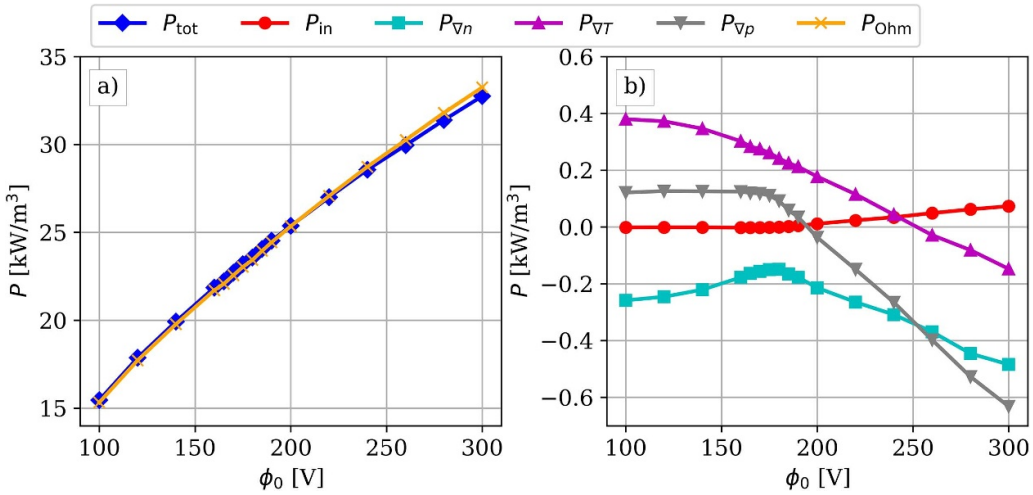

Figure 5. Spatio-temporally averaged electron power absorption as a function of voltage amplitude, ϕ_0. The total electron power absorption and the Ohmic term are presented in panel (a), while other power absorption terms, such as inertia, ambipolar, temperature gradient, and pressure gradient, are presented in panel (b). Discharge conditions: $L = 15$ mm, $p = 60$ Pa, $f = 13.56$ MHz.

The striated structure of the electron density leads to the peculiar shape of the ionization rate in panel (d): while traversing the discharge gap, electrons cross multiple striations and are accelerated more strongly by the striated electric field, whenever the local electron density increases along their direction of motion, while after reaching the local maximum of the electron density, they are decelerated, since the ambipolar electric field changes its sign. This is the reason for the alternating series of high and low ionization rate regions as a function of position, as seen in panel (d). We note the following point regarding terminology: comparing panels (c) and (d), the dominant ionization patterns in both the DA- and STR-modes are very similar and always caused mainly by drift and ambipolar electric field. From this, one could argue, that the striation mode should actually be called 'striated Drift-Ambipolar-mode'. Although it is more rigorous, due to the fact, that 'striation mode' has already become a widely used term for this specific discharge mode, we will stick to it in the rest of the manuscript.

In order to understand how electron power absorption changes as striations set in, figures 5(a) and (b) show the spatio-temporally averaged total electron power absorption as well as the individual terms calculated by the Boltzmann term analysis, as a function of the voltage amplitude. As shown in panel (a), the spatio-temporally averaged total power absorption, P_{tot}, monotonically increases as a function of the voltage amplitude, due to the higher power input to the discharge. The Ohmic term, P_{Ohm}, which is the dominant term for all cases considered here, also increases as a function of the voltage amplitude due to the fact, that a higher voltage amplitude leads to an increase in the number of inelastic collisions between electrons and the background gas. A more interesting behaviour can be observed in case of the other terms, as shown in panel (b). The temperature gradient term, $P_{\nabla T}$, exhibits a monotonic decrease with increasing voltage amplitude. The inertia term, P_{in}, is negligible up to $\phi_0 \approx 180$ V, after which it starts increasing, but remains small in absolute value. The ambipolar term $P_{\nabla n}$, while increasing monotonically until $\approx$180 V, reaches a local maximum near this point, after which a monotonic decrease is observed as a function of ϕ_0. Since, based on figure 2(c), 180 V is the amplitude value where striations first appear, this change in the behaviour of $P_{\nabla n}$ can clearly be attributed to the presence of striations. The pressure gradient term, $P_{\nabla p}$ (which is the sum of $P_{\nabla n}$ and $P_{\nabla T}$) shows a similar behaviour: before striations appear, it is constant while it decreases monotonically as the voltage amplitude is increased above 180 V.

By simply comparing the magnitudes of the space- and time-averaged power absorption terms in panels (a) and (b), we can see that Ohmic power absorption is dominant on average. The other terms represent only small corrections on the order of 1%, as shown later. However, these other power absorption terms have important spatio-temporal effects. As will become clear in the following discussion, the Ohmic term is always positive, while the other terms change sign in both time and position, some reaching local magnitudes far exceeding the local Ohmic term, and therefore contribute significantly to the spatiotemporal structure and the principal operation mechanism of the discharge.

The observed behaviour below 180 V is in line with previous investigations [8, 75]: Due to the DA-mode, the electron temperature is elevated in the bulk as a consequence of the Ohmic electric field there. In electropositive discharges, the ambipolar power absorption term is nonzero on space- and time average due to a temporal asymmetry in the electron temperature [7]: the ambipolar electric field accelerates electrons near sheath expansion, and decelerates them near sheath collapse, thereby leading to a temporal asymmetry that results in a positive $P_{\nabla n}$ on space- and time average. In case of electronegative discharges, due to the presence of the electropositive edge, this effect is attenuated, since due to the change in the density gradient, electrons, first accelerated during sheath

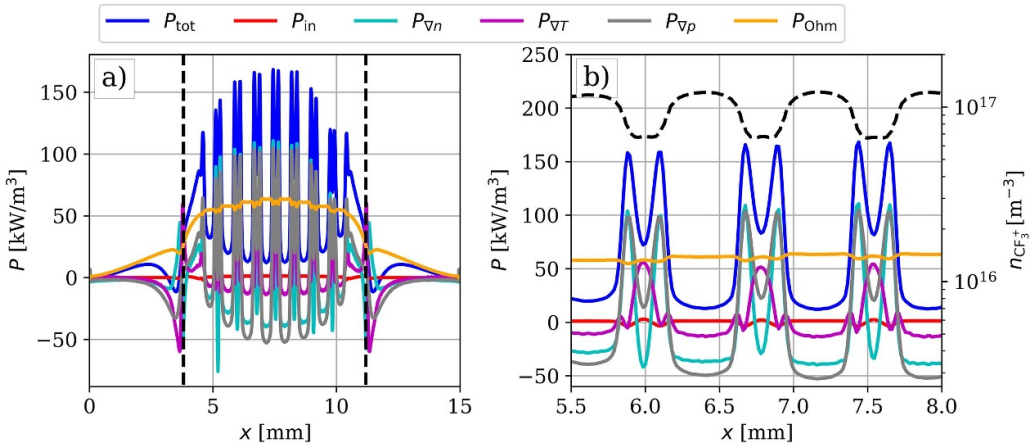

Figure 6. Time-averaged power absorption terms as well as total power absorption as a function of position for $\phi_0 = 300$ V for the whole discharge gap (a) and in the bulk between 5.5 mm and 8 mm (b). The vertical dashed black lines in panel (a) indicate the positions of the maximum sheath width s_{max}. In panel (b) the dashed black line indicates the time averaged CF_3^+ density (right y-axis). Discharge conditions: $L = 15$ mm, $p = 60$ Pa, $f = 13.56$ MHz.

expansion will be decelerated at the bulk side of the electropositive edge. Similarly, during sheath collapse, incoming electrons are accelerated first near the bulk side of the electropositive edge before being decelerated again. If the voltage amplitude is low, the acceleration from the ambipolar electric field during sheath expansion cannot increase the temperature to a high enough value (compared to the effect of the Ohmic electric field in the bulk), and therefore the temperature will be higher during sheath collapse, leading to a negative $P_{\nabla n}$ on space- and time average. If the voltage amplitude is increased, there will be a steeper increase of the electron density near the sheath expansion phase, and thus a higher $E_{\nabla n}$. This elevates the temperature, leading to a less negative $P_{\nabla n}$ on space- and time average, as seen in figure 5(b).

To investigate the electron power absorption dynamics in more detail in case of striations, figure 6 shows the temporally averaged electron power absorption terms as a function of position for the case when striations are pronounced, i.e. for $\phi_0 =$ 300 V, for the entire discharge gap (a) and for a region of the bulk (b). The maximum sheath width, s_{max}, is also included as black dashed vertical lines in figure 6(a). The Ohmic power absorption term has a high positive value in the bulk region due to the depleted electron density. The ambipolar and temperature gradient terms have maximum and minimum values, respectively, at the positions of maximum sheath width, s_{max}, which is a consequence of the presence of the electropositive edge (cf figure 4(b)).

In the bulk region, due to the presence of the striations, there is a double-peak structure for $P_{\nabla n}$, as shown in figure 6(b). Near the maxima of $P_{\nabla n}$, the Ohmic power absorption exhibits a local minimum: the reason for this is the local maximum of the electron density (cf figure 4(b)) as a result of the striations, which leads to an increased plasma conductivity and a smaller P_{Ohm}. The temperature gradient term, $P_{\nabla T}$ has as single positive peak between the maxima of $P_{\nabla n}$. The positivity of $P_{\nabla T}$ suggests that there is a local increase of the parallel temperature along the direction of the conduction current density, since, in order for a positive power absorption to take place, a

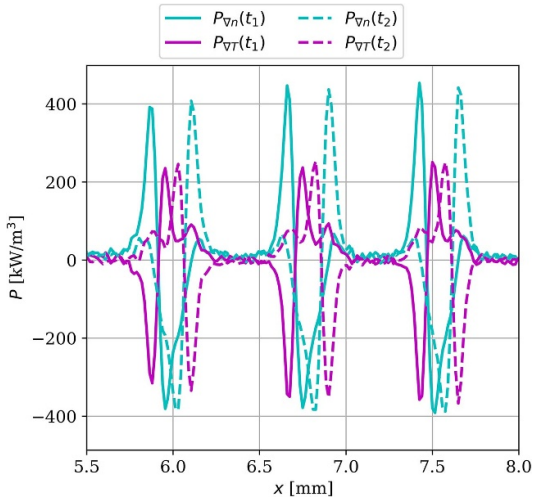

Figure 7. Ambipolar and temperature gradient electron power absorption terms ($P_{\nabla n}$, $P_{\nabla T}$, respectively) at the two time instances indicated in figure 4(b) for $\phi_0 = 300$ V. Discharge conditions: $L = 15$ mm, $p = 60$ Pa, $f = 13.56$ MHz.

negative electric field is needed for the electrons, which results in a positive temperature gradient (since $E_{\nabla T} \propto -\partial T_{\|}/\partial x$). This is evidently connected to the presence of the striations, since this peak appears multiple times in panel (b). Additionally, between each double-peak structure (i.e. between the density maxima of CF_3^+ and F^-), there is a considerable spatial region where $P_{\nabla n}$ is negative, whose spatial average will be negative in accordance with figure 5(b)).

In order to explain these structures, figure 7 shows $P_{\nabla n}$ and $P_{\nabla T}$ for the two specific time instances, t_1 and t_2 indicated previously in figure 4(b). As discussed there, these times are chosen such that the electron density is maximum near the edge of one of the neighbouring ion density (CF_3^+ or F^-) peaks. Based on figure 7, the presence of the double-peak structure in figure 6(b) (on time-average) is a consequence of the temporal modulation of the electron density: when there is

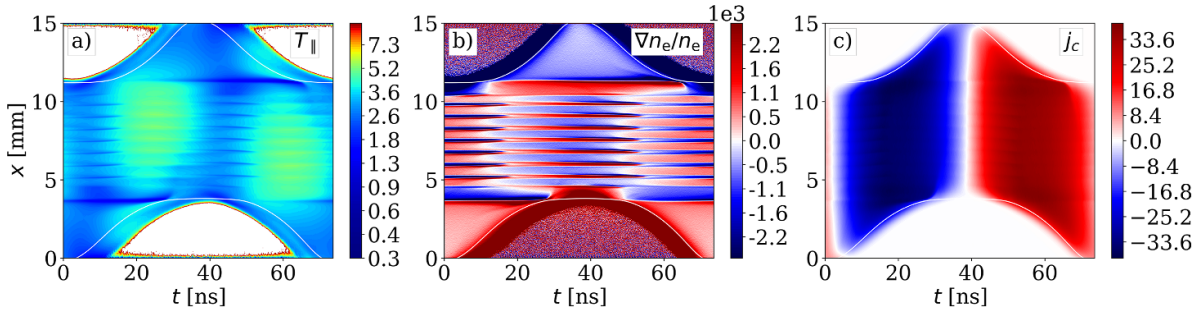

Figure 8. Spatio-temporal distribution of the electron temperature, $T_\parallel$, in units of eV (a), of the normalized electron density gradient, $\nabla n_e/n_e$, in units of m^{-1} (b) and of the electron conduction current density, j_c, in units of Am^{-2} (c) for 300 V. Discharge conditions: $L = 15$ mm, $p = 60$ Pa, $f = 13.56$ MHz.

a local maximum situated near the edge of a local ion density peak, there is a considerable density gradient with both negative and positive values, (somewhat like the electropositive edges near s_{max}). Since in one RF-cycle the density moves from one edge to the other, there are two distinct peaks for $P_{\nabla n}$, and the double-peak structure on time-average can be thought of as the sum of these contributions.

The positive peaks in figure 6(b) for $P_{\nabla T}$ can be explained based on similar grounds: the increase of $P_{\nabla n}$ means that the density gradient is positive, and thus the density increases (along the direction of the electron conduction current density). However, at first the gradient is not high enough, and thus the decrease of the Ohmic field cannot be compensated by the ambipolar electric field, the temperature decreases, leading to a negative $P_{\nabla T}$. When the density gradient reaches a high enough value (near one of the peaks of $P_{\nabla n}$ in figure 7), the local ambipolar electric field is already able to increase $T_\parallel$, leading to the change in $P_{\nabla T}$. This phase shift in space between the maxima/minima of the ambipolar and the temperature gradient power absorption terms is reflected in the close positive peaks shown in figure 7, that ultimately leads to the coalesced maximum in figure 6(b).

In order to understand the spatio-temporal behaviour of the ambipolar and temperature gradient terms in more detail, figure 8 shows the parallel electron temperature, $T_\parallel$ (a), the normalized electron density gradient, $\nabla n_e/n_e$ (b) and the electron conduction current density, j_c (c) for 300 V. As shown in panel (a), the electron temperature is locally decreased near the maxima of the electron density (cf figure 4(b)), due to the aforementioned mechanism, where the electron density gradient is not high enough to compensate the decrease of the Ohmic electric field due to the increased plasma conductivity. In accordance with what is usually observed in electronegative discharges [33, 76], the electron temperature is increased in the bulk whenever the bulk electric field is increased (at times when the electron conduction current density is high, cf panel (c)).

In addition to the Ohmic electric field in the bulk, due to the presence of the striations, regions of high ambipolar electric fields are present in the bulk, which locally increase/decrease the electron temperature depending on the spatial distribution of the electron density at a given time. This is shown in panel figure 8(b): At times when the electron density is maximum near the edges of the density maxima of CF_3^+ and F^-, the corresponding density gradient is considerable, leading to the peaks in $P_{\nabla n}$ discussed in figure 7. After the local maximum, the electron density decreases, due to the following reasons: (i) the increase of the CF_3^- density at positions where the CF_3^+ density is low, (ii) the recombination process between CF_3^+ and electrons as per table 3, and (iii) the drift of the electrons.

This leads to the wide spatial regions of negative/positive ∇n_e shown in figure 8(b), which leads to a high negative ambipolar power absorption. The reason for this is the following: the ambipolar field is proportional to $T_\parallel$, and as per figure 8(a), the temperature is considerable near the time of sheath expansion at either electrode. Comparing panels (b) and (c), in this temporal region the electron density gradient and the conduction current density are 'in phase', leading to a negative $P_{\nabla n}$ (which is $\propto -\nabla n_e$). Therefore, in the case of striations, there is no need for a temporal asymmetry in $T_\parallel$ in order to have a nonzero $P_{\nabla n}$ on time average, since the presence of the striations leads to a negative ambipolar power absorption on space-and time average. This is why the onset of striations leads to a decrease of $P_{\nabla n}$ in figure 5. If the voltage amplitude is increased, so are the ion densities, and therefore the region where the ambipolar power absorption is negative, increases, leading to the observed behaviour in figure 5.

The spatio-temporal distributions of each individual term contributing to electron power absorption are presented in figure 9. As shown in panel (a), the inertia term, P_{in}, is negligible compared to the other terms in absolute values. The ambipolar term, $P_{\nabla n}$ (panel (b)), shows high peaks near positions where the local electron density is maximum, and is mostly negative near positions where the electron conduction current density is high (due to the temporal modulation of the electron density and thus its gradient). The temperature gradient term, $P_{\nabla T}$ (c) has a similar structure to that of panel (b): near the local electron density maxima, in accordance with figure 7, there is a strong positive and negative peak for $P_{\nabla T}$, while at times when the electron conduction current density is high, $P_{\nabla T}$ has a strong positive and a weak negative region for each local ion density peak, due to the fact, that the Ohmic and ambipolar electric fields are superimposed, and the Ohmic electric field always increases the temperature (cf figures 8(a)

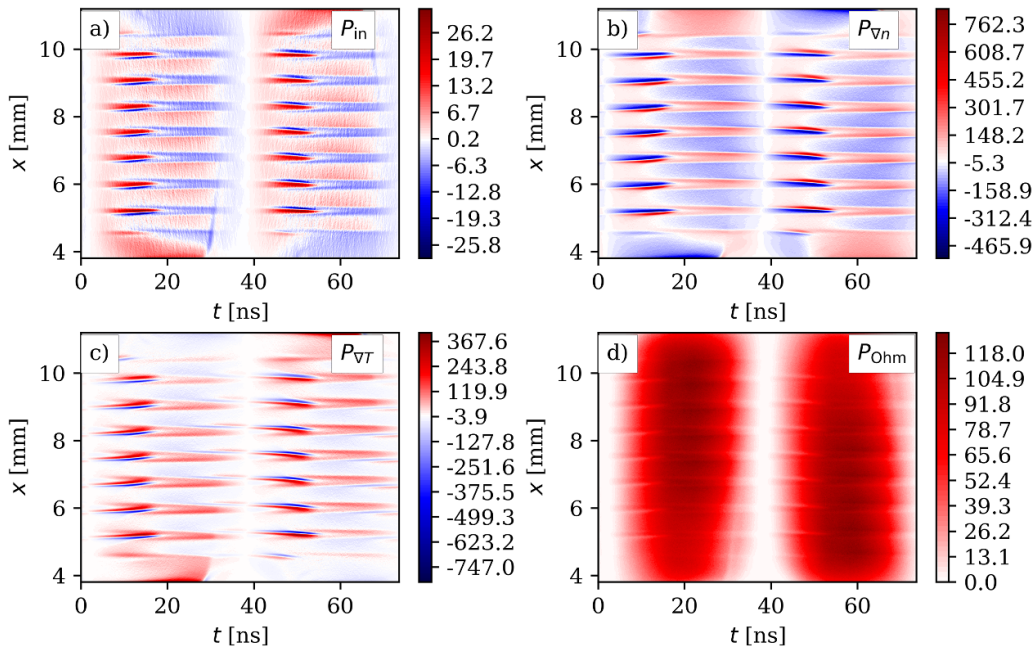

Figure 9. Spatio-temporal distribution of the electron power absorption terms in units of kW m^{-3} for $\phi_0 = 300$ V. Discharge conditions: $L = 15$ mm, $p = 60$ Pa, $f = 13.56$ MHz.

and 9 (d)). In other words, the temperature will be increased when both the Ohmic and the ambipolar field increase the electron energy, while if the ambipolar electric field changes sign, the decrease of the temperature will not be as high, since these two electric field terms are of the same order of magnitude. Figure 9(d) shows the Ohmic power absorption term, P_{Ohm}: the local decrease of this term, observed also in figure 6(b) is a consequence of the local increase in the electron density, due to which the plasma conductivity increases and thus P_{Ohm} decreases.

4. Conclusion

The electron power absorption mechanisms in electronegative capacitively coupled plasmas operated in CF_4 were investigated at a neutral gas pressure of 60 Pa and a driving frequency of 13.56 MHz, within a driving voltage amplitudes range of 100−300 V. The calculations were based on the Boltzmann term analysis, a method based on the electron momentum balance equation, which is capable of providing a complete spatio-temporal description of electron power absorption in CCRF discharges.

Under the conditions considered in this paper, the discharge was found to undergo a power absorption mode transition from the DA-mode to the striation mode at $\phi_0 = 180$ V. The presence of the striations leads to peculiarities in the ambipolar power absorption: due to the temporal modulation of the electron density and the high electronegativity, the ambipolar power absorption exhibits a strong positive and negative peak at positions when the electron density is maximum, while this term is negative in a wider spatial region between each local ion density peak. This leads to the striated structure observed in various physical quantities related to electrons, among others, the ionization rate and the parallel electron temperature. Due to the wide spatial region of negative ambipolar power absorption, the onset of striations is indicated by a local maximum in the spatio-temporally averaged ambipolar power absorption, as the voltage amplitude is increased. A notable difference in the spatio-temporal distribution of the ambipolar power absorption in case of striations, is that a temporal asymmetry in the electron temperature is no longer needed to have nonzero ambipolar power absorption on time average, since due to the presence of the striations the electron conduction current density and the ambipolar field are in phase with each other when the ambipolar electric field is high.

Data availability statement

The data that support the findings of this study are available upon reasonable request from the authors.

Acknowledgments

This work was supported by the National Office for Research, Development and Innovation (NKFIH) via Grant K134462 and by the German Research Foundation in the frame of the collaborative research center SFB 1316, Project A4, China Scholarship Council (No. 202106060085), by the Grant No. AP19679536 of the Ministry of Science and Higher Education of the Republic of Kazakhstan and by the J Bolyai Research Fellowship of the Hungarian Academy of Sciences.

ORCID iDs

Ranna Masheyeva https://orcid.org/0000-0002-6950-662X
Mate Vass https://orcid.org/0000-0001-9865-4982
Xiao-Kun Wang https://orcid.org/0000-0003-4160-5316
Yong-Xin Liu https://orcid.org/0000-0002-6506-7148
Aranka Derzsi https://orcid.org/0000-0002-8005-5348
Peter Hartmann https://orcid.org/0000-0003-3572-1310
Julian Schulze https://orcid.org/0000-0001-7929-5734
Zoltán Donkó https://orcid.org/0000-0003-1369-6150

References

[1] Lieberman M A and Lichtenberg A J 2005 *Principles of Plasma Discharges and Materials Processing* 2nd edn (Wiley Interscience)
[2] Makabe T and Petrovic Z L 2006 *Plasma Electronics: Applications in Microelectronic Device Fabrication* (CRC Press)
[3] Ohmori T and Makabe T 2008 *Appl. Surf. Sci.* **254** 3696–709
[4] Wilczek S, Schulze J, Brinkmann R P, Donkó Z, Trieschmann J and Mussenbrock T 2020 *J. Appl. Phys.* **127** 181101
[5] Chabert P and Braithwaite N 2011 *Physics of Radio-Frequency Plasmas* (Cambridge University Press)
[6] Surendra M and Dalvie M 1993 *Phys. Rev.* E **48** 3914
[7] Schulze J, Donko Z, Lafleur T, Wilczek S and Brinkmann R P 2018 *Plasma Sources Sci. Technol.* **27** 055010
[8] Vass M, Wilczek S, Lafleur T, Brinkmann R P, Donkó Z and Schulze J 2020 *Plasma Sources Sci. Technol.* **29** 025019
[9] Lafleur T, Chabert P and Booth J P 2014 *Plasma Sources Sci. Technol.* **23** 035010
[10] Vass M, Wilczek S, Lafleur T, Brinkmann R P, Donko Z and Schulze J 2020 *Plasma Sources Sci. Technol.* **29** 085014
[11] Proto A and Gudmundsson J T 2020 *J. Appl. Phys.* **128** 113302
[12] Proto A and Gudmundsson J T 2021 *Plasma Sources Sci. Technol.* **130** 065009
[13] Derzsi A, Hartmann P, Vass M, Horváth B, Gyulai M, Korolov I, Schulze J and Donkó Z 2022 *Plasma Sources Sci. Technol.* **31** 085009
[14] Wang L, Wen D Q, Hartmann P, Donkó Z, Derzsi A, Wang X F, Song Y H, Wang Y N and Schulze J 2020 *Plasma Sources Sci. Technol.* **29** 105004
[15] Zheng B, Wang K, Grotjohn T, Schuelke T and Fan Q H 2019 *Plasma Sources Sci. Technol.* **28** 09LT03
[16] Zheng B, Fu Y, Wang K, Schuelke T and Fan Q H 2021 *Plasma Sources Sci. Technol.* **30** 035019
[17] Vass M, Wilczek S, Schulze J and Donkó Z 2021 *Plasma Sources Sci. Technol.* **30** 105010
[18] Faraji F, Reza M and Knoll A 2022 *J. Appl. Phys.* **131** 193302
[19] Charoy T, Lafleur T, Tavant A, Chabert P and Bourdon A 2020 *Phys. Plasmas* **27** 3510
[20] Lafleur T and Chabert P 2017 *Plasma Sources Sci. Technol.* **27** 015003
[21] Kawamura E, Lieberman M and Lichtenberg A 2014 *Phys. Plasmas* **21** 123505
[22] Chabert P, Tsankov T V and Czarnetzki U 2021 *Plasma Sources Sci. Technol.* **30** 024001
[23] Popov O A and Godyak V A 1985 *J. Appl. Phys.* **57** 53
[24] Schulze J, Donkó Z, Luggenhölscher D and Czarnetzki U 2009 *Plasma Sources Sci. Technol.* **1870** 034011
[25] Godyak V and Khanneh A 1986 *IEEE Trans. Plasma Sci.* **14** 112–23
[26] Horváth B, Daksha M, Korolov I, Derzsi A and Schulze J 2017 *Plasma Sources Sci. Technol.* **26** 124001
[27] Boeuf J P 1987 *Phys. Rev.* A **36** 2782–92
[28] Schweigert I 2004 *Phys. Rev. Lett.* **92** 155001
[29] Gudmundsson J and Snorrason D 2017 *J. Appl. Phys.* **122** 193302
[30] Horváth B, Donkó Z, Schulze J and Derzsi A 2022 *Plasma Sources Sci. Technol.* **31** 045025
[31] Schulze J, Derzsi A, Dittmann K, Hemke T, Meichsner J and Donkó Z 2011 *Phys. Rev. Lett.* **107** 275001
[32] Liu G H, Liu Y X, Bai L S, Zhao K and Wang Y N 2018 *Phys. Plasmas* **25** 023515
[33] Liu Y X, Schüngel E, Korolov I, Donkó Z, Wang Y N and Schulze J 2016 *Phys. Rev. Lett.* **116** 255002
[34] Liu Y X, Korolov I, Schüngel E, Wang Y N, Donkó Z and Schulze J 2017 *Plasma Sources Sci. Technol.* **26** 055024
[35] Liu Y X, Donkó Z, Korolov I, Schüngel E, Wang Y N and Schulze J 2019 *Plasma Sources Sci. Technol.* **28** 075005
[36] Liu Y X, Korolov I, Schüngel E, Wang Y N, Donkó Z and Schulze J 2017 *Phys. Plasmas* **24** 073512
[37] Levitskii S M 1958 *Sov. Phys.-Usp.* **2** 887
[38] Godyak V, Piejak R and Alexandrovich B 1992 *Phys. Rev. Lett.* **68** 40–43
[39] Bohm C and Perrin J 1991 *J. Phys. D: Appl. Phys.* **24** 865
[40] Parker G, Hitchon W and Lawler J 1993 *Phys. Fluids* B **5** 646–9
[41] Derzsi A, Bruneau B, Gibson A R, Johnson E, O'Connell D, Gans T, Booth J P and Donkó Z 2017 *Plasma Sources Sci. Technol.* **26** 034002
[42] Gudmundsson J T and Ventjou B 2015 *J. Appl. Phys.* **118** 153302
[43] Gudmundsson J T and Proto A 2019 *Plasma Sources Sci. Technol.* **28** 045012
[44] Gudmundsson J T, Snorrason D I and Hannesdottir H 2018 *Plasma Sources Sci. Technol.* **27** 025009
[45] Derzsi A, Korolov I, Schüngel E, Donkó Z and Schulze J 2015 *Plasma Sources Sci. Technol.* **24** 034002
[46] Donkó Z, Derzsi A, Vass M, Schulze J, Schuengel E and Hamaguchi S 2018 *Plasma Sources Sci. Technol.* **27** 104008
[47] Wang L, Vass M, Donkó Z, Hartmann P, Derzsi A, Song Y H and Schulze J 2022 *Plasma Sources Sci. Technol.* **31** 06LT01
[48] Kolobov V 2006 *J. Phys. D: Appl. Phys.* **39** R487
[49] Kolobov V, Guzman J and Arslanbekov R 2022 *Plasma Sources Sci. Technol.* **31** 035020
[50] Golubovskii Y, Kolobov V and Nekuchaev V 2013 *Phys. Plasmas* **20** 1602
[51] Tahiyat M M, Stephens J C, Kolobov V I and Farouk T I 2021 *J. Phys. D: Appl. Phys.* **55** 085201
[52] Arslanbekov R R and Kolobov V I 2005 *IEEE Trans. Plasma Sci.* **33** 354–5
[53] Kawamura E, Lieberman M A and Lichtenberg A J 2017 *J. Phys. D: Appl. Phys.* **50** 145204
[54] Pollard W, Suzuki P and Staack D 2014 *IEEE Trans. Plasma Sci.* **42** 2650–1
[55] Nighan W L and Wiegand W 1974 *Phys. Rev.* A **10** 922
[56] Haas R A 1973 *Phys. Rev.* A **8** 1017–43
[57] Wang X K, Liu Y X, Wang X Y, Zhang Q Z, Zhao K and Wang Y N 2021 *Plasma Sources Sci. Technol.* **30** 055019
[58] Wang X K, Wang X Y, Liu Y X, Schulze J, Donkó Z and Wang Y N 2022 *Plasma Sources Sci. Technol.* **31** 064002
[59] Lisovskiy V, Dudin S and Yegorenkov V 2023 *Phys. Scr.* **98** 106101
[60] Donkó Z, Derzsi A, Vass M, Horváth B, Wilczek S, Hartmann B and Hartmann P 2021 *Plasma Sources Sci. Technol.* **30** 095017
[61] Donkó Z 2011 *Plasma Sources Sci. Technol.* **20** 024001
[62] Wang X K, Masheyeva R, Liu Y X, Hartmann P, Schulze J and Donkó Z 2023 *Plasma Sources Sci. Technol.* **32** 085009
[63] Denpoh K and Nanbu K 2022 *J. Vac. Sci. Technol.* A **40** 063007

[64] Denpoh K and Nanbu K 1998 *J. Vac. Sci. Technol.* A **16** 1201–6
[65] Donkó Z and Petrović Z L 2006 *Jpn. J. Appl. Phys.* **45** 8151–6
[66] Kurihara M, Petrovic Z L and Makabe T 2000 *J. Phys. D: Appl. Phys.* **33** 2146–53
[67] Bonham R A 1994 *Japan. J. Appl. Phys.* **33** 4157–64
[68] Georgieva V and Bogaerts A 2005 *J. Appl. Phys.* **98** 023308
[69] Georgieva V and Bogaerts A 2003 *J. Appl. Phys.* **93** 2369
[70] Denpoh K and Nanbu K 2000 *Jpn. J. Appl. Phys.* **39** 2804
[71] Nanbu K and Denpoh K 1998 *J. Phys. Soc. Japan* **67** 1288–90
[72] Rauf S and Kushner M J 1997 *J. Appl. Phys.* **82** 2805–13
[73] Vass M, Wilczek S, Lafleur T, Brinkmann R P, Donkó Z and Schulze J 2021 *Plasma Sources Sci. Technol.* **30** 065015
[74] Denpoh K 1998 Studies on CF4 Plasmas using Particle-based Simulation Models *PhD Thesis* Tohoku University, Sendai, Japan
[75] Vass M, Wilczek S, Derzsi A, Horváth B, Hartmann P and Donkó Z 2022 *Plasma Sources Sci. Technol.* **31** 045017
[76] Schulze J, Donko Z, Derzsi A, Korolov I and Schuengel E 2014 *Plasma Sources Sci. Technol.* **24** 015019